Electrochemical and Solid-State Letters, **14** (2) A14-A18 (2011)
1099-0062/2010/14(2)/A14/5/$28.00 © The Electrochemical Society

Numerical Simulation of the Effect of the Dissolution of $LiMn_2O_4$ Particles on Li-Ion Battery Performance

Jonghyun Park,[a] Jeong Hun Seo,[a] Gregory Plett,[b,*] Wei Lu,[a] and Ann Marie Sastry[a,c,d,z]

[a]*Department of Mechanical Engineering,* [c]*Department of Biomedical Engineering, and* [d]*Department of Materials Science and Engineering, University of Michigan, Ann Arbor, Michigan 48109-2125, USA*
[b]*Department of Electrical and Computer Engineering, University of Colorado at Colorado Springs, Colorado Springs, Colorado 80933-7150, USA*

Dissolution of active material is one of the primary reasons for capacity fade in lithium-ion batteries, particularly at elevated temperatures. The effects of the volume fraction changes due to dissolution in both the active and inert material phases in composite Li-ion electrodes are investigated by a thermal–electrochemical coupled model. The study reveals that the changes in effective transport properties result in a reduction in the electrochemical reaction rate and an increase in the cell resistance, reducing capacity. The simulation results are also used to map the nature of the effects of dissolution of the active particles on the capacity decrease during cycling with different conditions, including temperature and voltage range.
 [DOI: 10.1149/1.3516619]

Manuscript submitted September 3, 2010; revised manuscript received October 21, 2010. Published November 19, 2010.

Dissolution of Mn_2O_4 and Capacity Fade

Capacity fade in Li-ion batteries is one of the critical problems that must be resolved to realize practical power sources for electrical vehicles. Capacity fade is linked to a number of processes and their interactions, including electrochemical, chemical, and mechanical degradations, in both cathodes and anodes. The lithium manganese oxide spinel is a particularly promising cathode material because of its high voltage, low cost, and low environmental impact, but the material is apparently more vulnerable to cathode dissolution in an electrolyte[1-4] than other cathode materials. For example, weights of dissolved metal ions measured by atomic absorption spectroscopy (AAS) have been reported for $LiCoO_2$, $LiFePO_4$, and $LiMn_2O_4$ as 0.8, 0.5, and 3.2%.[5] Also, the amount of cobalt and nickel in the electrolyte was below the limit of detection after four week storage of lithium–nickel–cobalt mixed oxide in 1 M $LiPF_6$ with (ethylene carbonate/dimethyl carbonate) (EC/DMC) at 40°C.[6] Thus, study of cathode dissolution in $LiMn_2O_4$ is warranted in order to better mitigate the cathode dissolution and take better advantage of this high voltage, low-cost material.

Figure 1 shows a schematic diagram of the dissolution of manganese into the electrolyte, with associated mechanisms. The dissolution process occurs according to the disproportional reaction:[2,3,7,8] $2Mn^{3+} \rightarrow Mn^{4+} + Mn^{2+}$. The sequencing of these phenomena is as follows. Spinel particles begin dissolving, losing their intimate contact with conductive additive particles and increasing contact resistance. Electrode reaction resistance is increased due to the presence of dissolved Mn^{2+} ions in the electrolyte. The dissolved Mn^{2+} ions may be transported through the electrolyte to be deposited on the anode side. This phenomenon can deplete the anode by the reduction of Mn, which would oxidize Li in the anode.[9] This would also accelerate the capacity fade of Li-ion batteries.

The three main factors determining the dissolution rate are temperature, particle size, and operating voltage. The amount of the dissolved manganese ions has been observed to markedly increase with increasing temperature.[5,10] Particle size also plays an important role in determining the dissolution process. As the surface area increases for small particles, dissolution becomes more pronounced.[3] The elevated temperature performance of the $Li/LiMn_2O_4$ cell has been significantly improved using a spinel cathode with a small surface area.[11] Finally, the operating voltage is another important factor in determining the dissolution rate. An experiment using rotating ring-disk electrode techniques[12] has demonstrated that the dissolution of Mn from spinel $LiMn_2O_4$ occurs during charge/discharge cycling, especially in a charged state (at >4.1 V) and in a discharged state (at <3.1 V).

This observation in the high voltage region has been confirmed by in situ X-ray diffraction.[13] The two-phase structure coexisting in the high voltage region persists during lithium-ion insertion/extraction at low temperature during cycling. By contrast, this two-phase structure is effectively transformed to a more stable, one-phase structure, accompanied by the dissolution of Mn and the loss of oxygen at high temperature. The dissolution acceleration in the low voltage is due to the formation of a tetragonal phase $Li_2Mn_2O_4$. $Li_2Mn_2O_4$ is a Mn^{3+}-rich spinel, and so is more likely to dissolve into the electrolyte by the disproportional reaction described earlier.[14-16] While strictly limiting composition of $Li_xMn_2O_4$ within a range of $0 < x < 1$ may prevent the onset of the phase transition, an experiment[17] has observed phase boundaries separating the tetragonal phase at the surface of the crystallite from the cubic phase within the bulk in high voltage regions. At high current density, some crystallites at the surface can become overlithiated and then undergo phase transition even above 3 V.[14] This phase transition could be a problem for high power batteries being developed for electric vehicles.

Recent experiments support these assumptions. Increase in capacity loss and structural disorder at elevated temperature for small particles due to the process of manganese dissolution have been confirmed by AAS.[10]

Collectively, these efforts link capacity fade to cathode particle dissolution and strongly imply that small particles dissolve in both high and low voltage regions. However, a quantitative understanding between dissolution and capacity fade through a physics-based model has not yet been reported. The present work is focused on modeling the effect of dissolution on performance degradation in Li-ion batteries via a physics-based thermal–electrochemical model. In this study, we have the following objectives:

1. Derive volume fraction changes in electrodes due to dissolution and extend the porous electrode theory to correlate dissolution with capacity fade in Li-ion batteries.
2. Map the nature of the effects of dissolution on the capacity decrease during cycling with different conditions, including temperature and voltage range.

Volume Changes in Cathode due to Material Loss

Figure 2 shows a schematic diagram of the dissolution process described earlier. The Mn^{3+} ions residing in the original spinel structure gradually convert into Mn^{4+} and Mn^{2+}, whereas the Mn^{4+} ions

* Electrochemical Society Active Member.
z E-mail: amsastry@umich.edu

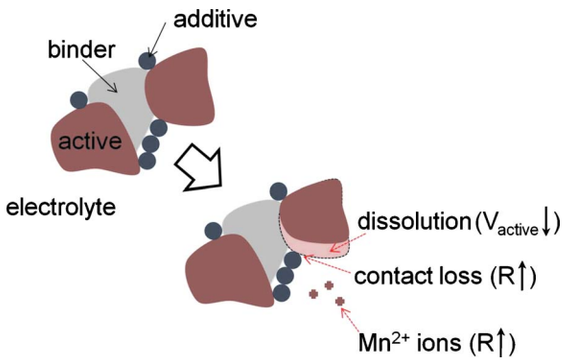

Figure 1. (Color online) Schematic diagram of the effect of dissolution.

remain in the solid structure, and the Mn^{2+} ions gradually dissolve into the electrolyte. The dissolution process can be modeled via the noncatalytic reaction of particles with a surrounding medium, which is referred to as the shrinking unreacted-core model.[18] AAS measurement has verified that the model based on the reaction of a fluid with a solid at the reaction surface holds among three different mechanisms.[10] In that model, the function of dissolution ratio and reaction time is expressed by

$$[1 - (1 - X_a)^{1/3}] = kt \quad [1]$$

where k is constant, t is time, and X_a is the dissolution reaction defined as two times the amount of Mn^{2+} ions in the electrolyte compared to Mn^{3+} ions in the original powder. From the dissolution reaction rate, the volume reduction can be derived as

$$\frac{M_d^{3+}}{M_i^{3+}} = \frac{X_a}{1 + X_a}, \quad M_a^{4+} = \frac{1}{2}M_d^{3+} \quad [2]$$

where M_i^{3+}, M_d^{3+}, and M_r^{4+} represent the initial Mn^{3+}, dissolved Mn^{3+}, and remaining Mn^{4+} molar mass, respectively. From the expressions of molar mass ratios of Li^+, Mn^{3+}, Mn^{4+}, and O^{2-} and atomic weight ratio ($Mn/LiMn_2O_4 = 0.304$), the volume at time t can be calculated as

$$V(t) = V_i\left(1 - \frac{0.304}{2}\frac{X_a}{X_a + 1}\right) \quad [3]$$

where V_i represents the initial volume. Here, we only consider volume change due to manganese loss and assume that the loss is compensated via an increase in the inert volume. Consequently, the changes of the volume fraction of the cathode active material (ε_{active}) and inert material (ε_{inert}) are

$$\varepsilon_{active} = \varepsilon^i_{active}\left(1 - \frac{0.304}{2}\frac{X_a}{X_a + 1}\right) \quad [4]$$

$$\varepsilon_{inert} = \varepsilon^i_{inert} + \varepsilon^i_{active}\frac{0.304}{2}\frac{X_a}{X_a + 1} \quad [5]$$

where ε^i_{active} and ε^i_{inert} are the initial volume fraction values of the cathode active material and inert material, respectively. Relative volume changes in each phase alter the effective diffusivity and conductivity of the electrodes and the specific area of the cathode material. As a result, the chemical reaction between the solid and electrolyte is also affected. As mentioned earlier, the amount of dissolved manganese ions is a function of temperature. The standard Arrhenius representation, $k = k_0 \exp(-E_a/RT)$, for reaction rate is used to include the temperature effect. Here, k_0 is the frequency factor, E_a is the activation energy, T is the temperature, and R is the gas constant.

The volume fraction changes in composite electrodes can affect the specific interfacial area and the effective transport properties in

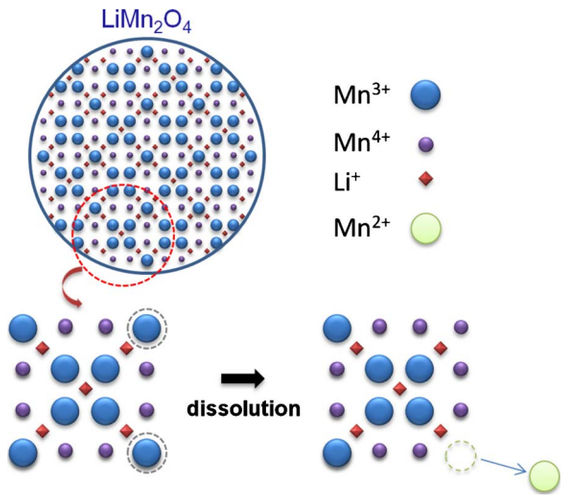

Figure 2. (Color online) Schematic diagram of the dissolution process: two Mn^{3+} cations convert into one Mn^{4+} and one Mn^{2+}, then Mn^{2+} ions leave the solid phase.

the mathematical modeling of Li-ion batteries. The coupled thermal–electrochemical model based on the volume-averaged porous theory, which is summarized below, is applied to study the effect of the volume change due to manganese dissolution. Conservation of charge in the solid and electrolyte phases yields

$$\nabla \cdot (\sigma_s^{eff} \nabla \phi_s) - J^{Li} = 0 \quad [6]$$

$$\nabla \cdot \left(\kappa_e^{eff}\left(\nabla \phi_e - \frac{2RT}{F}(1 - t_+^0)\left(1 + \frac{d \ln f_{\pm}}{d \ln c_e}\right)\nabla \ln c_e\right)\right) + J^{Li} = 0 \quad [7]$$

The material balance in the electrolyte yields

$$\frac{\partial(\varepsilon_e c_e)}{\partial t} = \nabla \cdot (D_e^{eff} \nabla c_e) + \frac{1 - t_+^0}{F}J^{Li} - \frac{i_e \cdot \nabla t_+^0}{F} \quad [8]$$

Fickean diffusion describes the transport in the spherical particles

$$\frac{\partial c_s}{\partial t} + \frac{1}{r^2}\nabla (r^2 D_s \nabla c_s) = 0 \quad [9]$$

In Eq. 6-9 rate equation is needed to determine the reaction rates for the insertion and deinsertion reactions. We assume that it follows the Butler–Volmer equation, namely

$$J^{Li} = a_s k(\bar{c}_{se})^{\alpha_c}(c_{s,max} - \bar{c}_{se})^{\alpha_a}(c_e)^{\alpha_a}\left(\exp\left(\frac{\alpha_a F}{RT}\eta\right) - \exp\left(-\frac{\alpha_c F}{RT}\eta\right)\right) \quad [10]$$

where c stands for the volume-averaged lithium concentration and subscripts e and s refer to the electrolyte and solid phases, respectively. $\bar{c}_{se}$ represents the area-averaged solid state lithium concentration at the solid-electrolyte interphase, and the specific interfacial surface a_s can be written as

$$a_s = \frac{3\varepsilon_{active}}{R_s} \quad [11]$$

The decreased active material volume fraction results in an increase of the effective resistance in the solid phase as follows

$$\sigma_s^{eff} = (\varepsilon_{active})^{1.5}\sigma_s \quad [12]$$

Thermal energy conservation can be expressed by

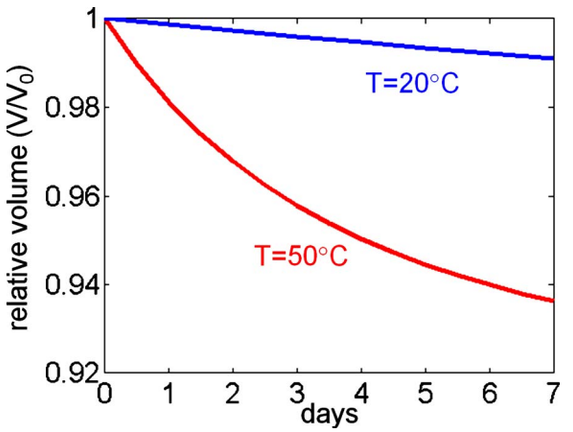

Figure 3. (Color online) Volume change due to dissolution at different temperatures.

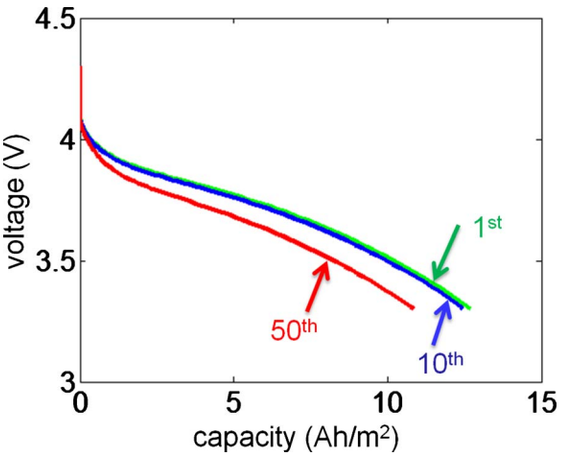

Figure 4. (Color online) Discharge voltage profiles for different numbers of cycles.

$$\frac{\partial(\rho c_p T)}{\partial t} = \nabla \cdot \lambda \nabla T + q \qquad [13]$$

Here, the heat generation rate includes heat effect due to the electrode reaction, joule heating, and entropy change of the electrode reaction, which is expressed by

$$q = J\left(\phi_s - \phi_e - U_j + T\frac{\partial U_j}{\partial T}\right) + \sigma_s^{\text{eff}} \nabla \phi_s \cdot \nabla \phi_s + (\kappa_e^{\text{eff}} \nabla \phi_e \cdot \nabla \phi_e + \kappa_e^{D} \nabla \ln c_e \cdot \nabla \phi_e) \qquad [14]$$

Here, the first term of the right-hand side of Eq. 14 represents the heat sources due to charge transfer at the electrode/electrolyte interfaces and the entropy change. The last two terms arise from the joule heating in the solid active and electrolyte phases, respectively.

Results: Volume Change, Dissolution, and Temperature Linkages

To study the effect of the volume change due to manganese dissolution, a Li-ion battery composed of graphite anode (100 μm) and manganese oxide ($LiMn_2O_4$) cathode (183 μm) is studied. The electrolyte contains 1 M of $LiPF_6$ in EC:DMC solvent. The particle size in the cathode material is 19.9 μm in diameter. The other parameters used here are the same as those used in prior work.[19,20] The dissolution rate is obtained experimentally[10] using the Arrhenius relation. The activation energy, E_a, is 72.84 kJ/mol, and the reference rate is $k_0 = 3.41 \times 10^5$ s^{-1}. To include the voltage effect during cycling above 4.1 V and below 3.1 V, an elevated reaction rate of 2.8 times is used, as observed experimentally.[13]

By varying the temperature and the upper and lower voltage limits during cycling, the effect of volume fraction changes on the capacity fade is determined. Figure 3 shows the volume changes due to the dissolution during storage. At 50°C, the volume change increases seven times more than that at 20°C. The results here are quite consistent with an experimental observation[13] in which the volume increased by 7.5 times. To elucidate the battery capacity changes during battery cycling, galvanostatic charge/discharge simulations with a limited voltage range are conducted. Figure 4 shows the representative discharge profiles. The battery is cycled at a C/2 rate between 3.3 and 4.3 V at 40°C. The capacity is around 13 Ah/m^2 at the first cycle, which is lower than the value (15 Ah/m^2) given in the reference. The larger active material particle size in the present work results in a lower capacity utilization due to diffusion limitations; the particle size in the present work is 19.9 μm, whereas the particle size in the reference[20] is 17 μm. After 50 cycles, the capacity decreases by 15%.

The active material loss causes a delay in the reaction rate for insertion and deinsertion at the solid and electrolyte phase boundary, which results in an increase in resistance. To verify the increase in resistance, the discharge resistances are calculated using $\Delta V/\Delta I$ calculation after applying a short current pulse (120 s). We compensated for voltage shift by removing the contribution of the voltage drop due to state of charge (SOC) change. The voltage drop due to the SOC change was calculated from the relaxation voltages before and after applying the short current. Figure 5 shows the relative resistance for different cycle numbers. The resistance increases 1.2 times after 50 cycles. The results of an ac impedance study[3] revealed that the manganese dissolution resulted in an increase in the contact resistances and also in the electrode reaction resistance for Li-ion (de)intercalation. In the study the resistance doubles after 35 cycles, which is a larger increase than that in the current results. This difference may come from the authors' explanation that the manganese dissolution is related to carbon content in the composite cathodes; the Mn dissolution increased with increasing carbon content in the composite electrode. It was proposed that the solvent molecules were electrochemically oxidized on the carbon surface and the by-product promoted the Mn dissolution. Also, the experimental temperature may have been different from that of our simulation, because it was not revealed in the reference. An increase in resistance will cause a high polarization, resulting in apparent capacity losses.

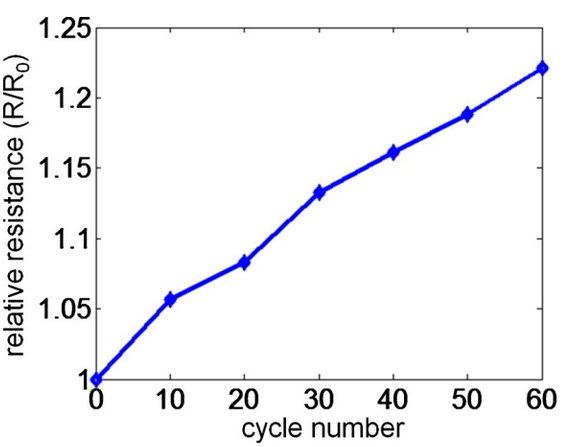

Figure 5. (Color online) Resistance changes for different numbers of cycles.

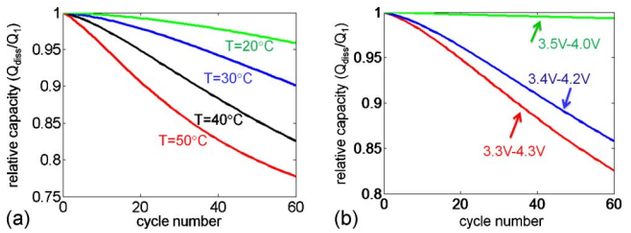

Figure 6. (Color online) Relative capacity decrease due to dissolution with (a) different temperature and (b) different voltage range.

Figure 6 shows the cycling results with different temperature and voltage ranges. Due to a higher temperature and a wider range of voltages, greater dissolution of cathode particles was shown to result in a severe capacity fade using the models derived here. The capacity fade increases by a factor of 5 when the temperature increases by 30°C after 60 cycles, and the cycling with a wider voltage range results in a 25% increase in the capacity fade after 60 cycles. These tendencies have already been demonstrated from several experimental observations. The capacity decreases 19% from 130 to 105 mAh/g after 50 cycles at 50°C for a $Li/LiMn_2O_4$ coin cell at a current rate of C/3 between 3.5 and 4.5 V.[13] In another experiment,[21] the capacity decreases about 23% from 118 to 90 mAh/g after 50 cycles at 50°C for a sample $Li[Li_{0.01}Mn_{1.99}]O_4$ operated in voltages between 3.5 and 4.5 V at a rate of 1 mA/cm^2. The capacity decrease in the present simulation is about 20% after 50 cycles at 50°C, which is similar to the above experimental observations.

Conclusions

Capacity fade occurs due to several mechanisms, including active material dissolution, passive film formation, and electrolyte decomposition. In this work, capacity fade due to the dissolution of cathode particles was studied numerically, using experimentally derived parameters. By evaluating the volume fraction changes in the solid phase due to dissolution, the changes in effective transport properties and electrochemical kinetics were incorporated into a one-dimensional thermoelectrochemical model. This provides a quantitative relationship between the volume fraction change and capacity fade. As simulation results demonstrate, the material loss of the active particle alone cannot fully account for the capacity loss. The material loss of the active particle results in decreased effective transport properties in the solid phase, which in turn results in a reduction in the electrochemical reaction rate, reducing capacity. Also, cycling simulations demonstrates that the capacity fade is accelerated with a higher temperature and a wider voltage range, which have been observed separately in several experiments.

The current results can be extended by including the resistance changes due to dissolution and other degradation mechanisms such as gas evolution,[22] which would provide a more comprehensive guide for studying capacity fade in Li-ion batteries. In the future, resistance change due to dissolution, if it is incorporated into this model, would provide a clear understanding of the effect of the dissolution of active particles on battery performance. We further aim to combine this work with simultaneous studies of other capacity degradation mechanisms in order to reduce the capacity losses in Li-ion batteries by an improved design of structures and materials.

Acknowledgments

This effort was supported by the General Motors/University of Michigan Advanced Battery Coalition for Drivetrains, with additional sponsorship by the Department of Energy and the Michigan Economic Development Corporation. The authors appreciate the support from their sponsors.

University of Michigan assisted in meeting the publication costs of this article.

List of Symbols

a_s	surface area of active material per volume of electrode, (m^{-1})
c_e	concentration of salt in the electrolyte, mol/m^3
c_p	specific heat, J/kg K
c_s	concentration of lithium in the solid electrode, mol/m^3
$c_{s,max}$	maximum concentration of lithium in the solid electrode, mol/m^3
D_e	diffusion coefficient of lithium in the electrolyte, m^2/s
D_s	diffusion coefficient of lithium in the solid electrode particle, m^2/s
$f_\pm$	mean molar activity coefficient of salt
F	Faraday's constant, 96,487 C/mol
$\mathbf{i}_e$	ionic current density in the electrolyte phase
k	reaction rate constant
M	molar mass, Kg/mol
q	volumetric heat generation rate, J/m^3 s
r	radial position across a spherical particle, m
R	universal gas constant, 8.3143 J/mol K
R_s	radius of a solid particle, m
t	time, s
t^0	transference number of Li-ion with respect to the solvent velocity
T	temperature, K
V	volume, m^3
X_a	dissolution reaction rate

Greek

α_a	anodic transfer coefficient
α_c	cathodic transfer coefficient
ε	volume fraction
η	potential difference at the solid-electrolyte interphase, V
κ	ionic conductivity of electrolyte, S/m
λ	thermal conductivity, W/m K
σ	electronic conductivity of solid matrix, S/m
ϕ	electric potential, V

Subscript

a	anodic
c	cathodic
d	dissolved ion
e	electrolyte (i.e., solution phase)
r	remaining ion
s	solid phase

Superscript

0	solvent
D	diffusional property
eff	effective material properties accounting for porous medium
i	initial value

References

1. S. J. Wen, T. J. Richardson, L. Ma, K. A. Striebel, P. N. Ross, and E. J. Cairns, *J. Electrochem. Soc.*, **143**, L136 (1996).
2. R. J. Gummow, A. de Kock, and M. M. Thackery, *Solid State Ionics*, **69**, 59 (1994).
3. D. H. Jang, Y. J. Shin, and S. M. Oh, *J. Electrochem. Soc.*, **143**, 2204 (1996).
4. Y. Xia and M. Yoshio, *J. Electrochem. Soc.*, **143**, 825 (1996).
5. W. Choi and A. Manthiram, *J. Electrochem. Soc.*, **153**, A1760 (2006).
6. M. Wohlfarht-Mehrens, C. Vogler, and J. Garche, *J. Power Sources*, **127**, 58 (2004).
7. E. Wang, D. Ofer, W. Bowden, N. Iltchev, R. Moses, and K. Brandt, *J. Electrochem. Soc.*, **147**, 4023 (2000).
8. T. Soshima, K. Okahara, C. Kiyohara, and K. Shizuka, *J. Power Sources*, **97–98**, 377 (2001).
9. K. Edstrom, T. Gustafsson, and J. O. Thomas, *Electrochim. Acta*, **50**, 397 (2004).
10. C.-H. Lu and S.-W. Lin, *J. Mater. Res.*, **17**, 1476 (2002).
11. Y. Xia, N. Kumada, and M. Yoshio, *J. Power Sources*, **90**, 135 (2000).
12. L.-F. Wang, C.-C. Ou, K. A. Striebel, and J.-S. Chen, *J. Electrochem. Soc.*, **150**, A905 (2003).
13. Y. Xia, Y. Zhou, and M. Yoshio, *J. Electrochem. Soc.*, **144**, 2593 (1997).
14. M. M. Thackeray, Y. Shao-Horn, A. J. Kahaian, K. D. Kepler, E. Skinner, J. T. Vaughery, and S. A. Hackney, *Electrochem. Solid-State Lett.*, **1**, 7 (1998).
15. A. Blyr, C. Sigala, G. G. Amatucci, D. Guyomard, Y. Chabres, and J. M. Tarascon, *J. Electrochem. Soc.*, **145**, 194 (1998).

16. G. Pistoia, A. Antonini, R. Rosati, C. Bellitto, and G. M. Ingo, *Chem. Mater.*, **9**, 1443 (1997).
17. M. M. Thackeray, *Prog. Solid State Chem.*, **25**, 1 (1997).
18. O. Levenspiel, *Chemical Reaction Engineering*, John Wiley & Sons, New York (1972).
19. W. B. Gu and C. Y. Wang, in *Lithium Batteries*, R. A. Marsh, Z. Ogumi, J. Prakash, and S. Surampudi, Editors, PV 99–25, p. 748, The Electrochemical Society Proceedings Series, Pennington, NJ (1999).
20. M. Doyle, J. Newman, A. S. Gozdz, C. N. Schmutz, and J. M. Tarascon, *J. Electrochem. Soc.*, **143**, 1890 (1996).
21. E. Iwata, K.-i. Takahashi, K. Maeda, and T. Mouri, *J. Power Sources*, **81**, 430 (1999).
22. J. H. Seo, J. Park, G. Plett, and A. M. Sastry, *Electrochem. Solid-State Lett.*, **13**, A135 (2010).